Coupled Aerosol-Cloud Systems over Northern Vietnam during 7-SEAS/BASELInE: A Radar and Modeling Perspective

Adrian M. Loftus[1,2]*, **Si-Chee Tsay[2]**, **Peter Pantina[2,3]**, **Cuong Nguyen[4,5]**, **Philip M. Gabriel[5,6]**, **Xuan A. Nguyen[7]**, **Andrew M. Sayer[2,8]**, **Wei-Kuo Tao[2]**, **Toshi Matsui[1,2]**

[1] *University of Maryland, College Park, Maryland, USA*

[2] *NASA Goddard Space Flight Center, Greenbelt, Maryland, USA*

[3] *Science Systems and Applications Inc., Lanham, Maryland, USA*

[4] *National Research Council, Ottawa, Ontario, Canada*

[5] *Colorado State University, Fort Collins, Colorado, USA*

[6] *General Analytics L.L.C., Fort Collins, Colorado, USA*

[7] *Vietnam Academy of Science and Technology, Hanoi, Vietnam*

[8] *GESTAR/USRA, Columbia, Maryland, USA*

ABSTRACT

The 2013 7-SEAS/BASELInE campaign over northern Southeast Asia (SEA) provided, for the first time ever, comprehensive ground-based W-band radar measurements of the low-level stratocumulus (Sc) systems that often exist during the spring over northern Vietnam in the presence of biomass-burning aerosols. Although spatially limited, ground-based remote sensing observations are generally free of the surface contamination and signal attenuation effects that often hinder space-borne measurements of these low-level cloud systems. Such observations permit detailed measurements of structures and lifecycles of these clouds as part of a broader effort to study potential impacts of these coupled aerosol-cloud systems on local and regional weather and air quality. Introductory analyses of the W-band radar data show these Sc systems generally follow a diurnal cycle, with peak occurrences during the nighttime and early morning hours, often accompanied by light precipitation. Preliminary results from idealized simulations of Sc development over land based on the observations reveal the familiar response of increased numbers and smaller sizes of cloud droplets, along with suppressed drizzle formation, as aerosol concentrations increase. Slight reductions in simulated W-band reflectivity values also are seen with increasing aerosol concentrations and result primarily from decreased droplet sizes. As precipitation can play a large role in removing aerosol from the atmosphere, and thereby improving air quality locally, quantifying feedbacks between aerosols and cloud systems over this region are essential, particularly given the negative impacts of biomass burning on human health in SEA. Such an endeavor should involve improved modeling capabilities along with comprehensive measurements of time-dependent aerosol and cloud profiles.

Keywords: Aerosol-cloud interactions; Radar observations; 7-SEAS; Cloud modeling.

BACKGROUND AND MOTIVATION

Aerosols are omnipresent in Earth's atmosphere and central to many environmental concerns such as air quality and climate change. During boreal spring in Southeast Asia (SEA), biomass-burning from natural forest fires and slash-and-burn agricultural practices strongly modulates the atmospheric composition over northern SEA (Lin *et al.*, 2013; Reid *et al.*, 2013, Tsay *et al.*, 2016, and references therein). The chemical and aerosol species associated with the

burning degrade the regional air quality and trigger adverse health effects in the local population (*cf*., Huang *et al.*, 2013; Lin *et al.*, 2014), and can additionally alter the lifecycles of clouds and distribution of precipitation through radiative and microphysical effects (Graf *et al.*, 2009; Lee *et al.*, 2014).

Satellite and ground-based observations of biomass-burning (BB) aerosols over SEA exhibit consistent spatiotemporal distribution patterns, with considerable variability due primarily to factors ranging from large-scale climatic influences (e.g., ENSO) to small-scale meteorological events (Gautam *et al.*, 2013; Reid *et al.*, 2013; Sayer *et al.*, 2016). Downwind from source regions, the transported and local BB aerosols often overlap with low-level stratocumulus (Sc) cloud decks (Hsu *et al.*, 2003; Tsay *et al.*, 2013) associated with the development of the region's pre-monsoon

(February–April) cloud and rain system (Fig. 1(a)). Analyses of Cloud-Aerosol Lidar and Infrared Pathfinder Satellite Observation/Cloud-Aerosol Lidar with Orthogonal Polarization (CALIPSO/CALIOP) vertical feature mask (Winker *et al.*, 2009) Version 3 data for the months of March and April from 2007–2014 depict the vertical frequency distribution of aerosols and clouds within a 2 × 2° box over northern Vietnam (Fig. 1(b)). A persistent aerosol layer peaking near 3 km above sea level is evident, whereas cloud top heights range mainly between 2 and 3 km. Increased occurrences of low-level cloudiness and an apparent overlap of the cloud layer top with the aerosol layer at night compared to daytime are also evident for both months and imply a diurnal cycle. However, significant attenuation of the lidar signal by clouds and heavy aerosol loading can lead to biases in feature detection capability in the boundary layer (Winker *et al.*, 2009).

Biomass-burning aerosols have also been recognized as effective cloud condensation nuclei (CCN, e.g., Crutzen and Andreae, 1990; Reid *et al.*, 2005; Engelhart *et al.*, 2012). They are particularly active at lower supersaturation levels, such as those occurring in Sc clouds, where aerosol-cloud interactions are most favored (e.g., Platnick and Twomey, 1994; Sorooshian *et al.*, 2009). Cloud precipitation processes (i.e., droplet self-collection, collision-coalescence) are modulated by CCN size, and to a lesser extent composition (Dusek *et al.*, 2006; Reutter *et al.*, 2009; Feingold *et al.*, 2013). In general, the impacts of increasing aerosol/CCN concentrations on clouds tend to decrease cloud particle size and increase particle number, and thereby potentially suppress precipitation (Twomey, 1977; Albrecht, 1989; Ackerman *et al.*, 2004). However, BB aerosols located within the boundary layer over land may increase convective

cloudiness associated with aerosol-induced boundary layer warming and could lead to stronger convection and greater rainfall rates (Feingold *et al.*, 2005; Martins *et al.*, 2009).

Aerosol impacts on low-level Sc over land remain unclear given that far less attention has been paid to these clouds compared to marine Sc (*cf.* Klein and Hartmann, 1993; Lin *et al.*, 2014), presumably given the critical role of the latter in modulating radiant energy and latent heat that affect weather and climate (Stephens and Greenwald, 1991; Lohmann and Feichter, 2005; Wood, 2012). Indeed, the semi-persistent low-level Sc systems that exist over northern Vietnam from November through April offer a unique opportunity to investigate a myriad of possible feedbacks between these cloud systems and BB aerosols. During winter and early spring, low-level Sc cloud layers consistently form over the South China Sea/East Sea and Gulf of Tonkin under conditions of broad subsidence and lower-tropospheric stability associated with a local Hadley circulation (Klein and Hartmann, 1993). The cloud layers often extend into southeast China and northern Vietnam as the prevailing low-level flow southwest of the East Asian anticyclone advects moisture inland beneath a strong inversion. Drizzle from these clouds frequently occurs over north and north-central Vietnam from mid-winter into the pre-monsoon months (Nguyen and Nguyen, 2004). Decreasing trends in rainfall over the past 50+ years for this region (Fig. 2) are consistent with recent regional climate trends (Endo *et al.*, 2009; Nguyen *et al.*, 2010; Ho *et al.*, 2011; Phan *et al.*, 2014; Schmidt-Thomé *et al.*, 2015), and it is believed that increased BB aerosol loading during the spring may be partially responsible. The removal of atmospheric aerosols by nucleation and precipitation scavenging processes mitigate local and regional air quality in addition to potential
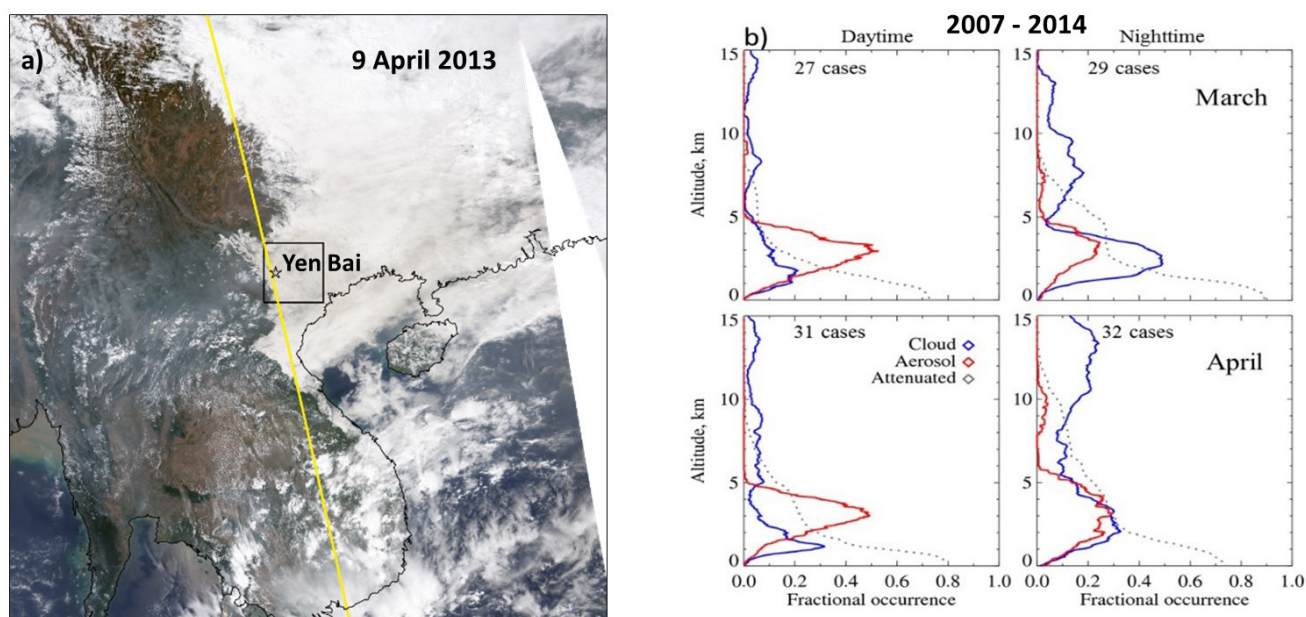

Fig. 1. a) Aqua/MODIS RGB image on 9 April 2013 covering the region 10–30°N, 96–116°E superimposed with A-Train overpass (yellow line) track, and b) CALIPSO/CALIOP Version 3 aerosol and cloud vertical frequency distributions within a 2 × 2 degree sub-domain (grey box in panel a) for March (top row) and April (bottom row) partitioned by daytime (left column) and nighttime (right column) overpasses for the years 2007–2014.
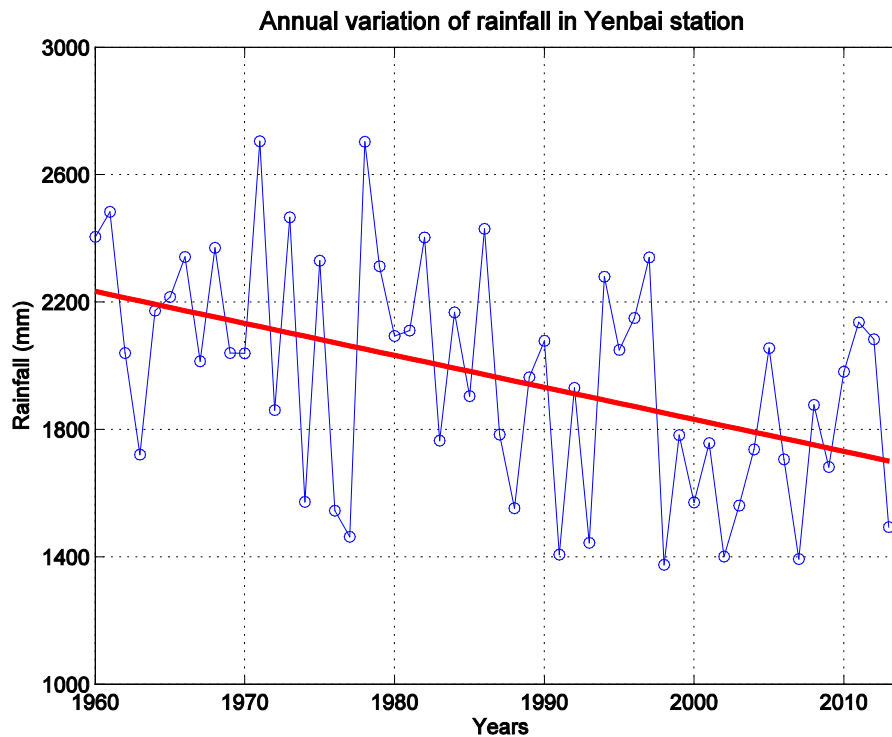
Annual variation of rainfall in Yenbai station

Fig. 2. Annual rainfall amounts (blue line) recorded at the Yen Bai meteorological station for the years 1960–2013. The bold red line depicts the trend over the same time period. Data courtesy of The Ministry of Natural Resources and Environment, Socialist Republic of Vietnam.

effects on cloud and precipitation evolution downstream (Pruppacher and Klett, 1997; Levin and Cotton, 2009). Thus, it is probable that if precipitation suppression due to enhanced aerosol loading occurs over northern SEA, this could act to exacerbate the poor air quality conditions often observed over the region during the spring.

A better understanding of aerosol-cloud-precipitation interactions over SEA naturally entails detailed observations of the cloud systems in the region. Multi-wavelength radars, and cloud radars in particular, present the most relevant platforms for obtaining comprehensive 3-D cloud structure, as well as composition and evolution (*cf.* Clothiaux *et al.*, 1995; Baab *et al.*, 1999; Kollias *et al.*, 2007, Tridon *et al.*, 2013 and references therein). The Cloud Profiling Radar (CPR) aboard CloudSat (Stephens *et al.*, 2002), for example, has a vertical resolution of about 500 m (240 m for oversampled bin centers) and is the first space-borne radar to measure the vertical structure of clouds and light precipitation. However, the most significant difficulty with the CloudSat/CPR is that surface clutter effectively reduces the radar sensitivity such that detection of moderate drizzle over oceans is limited to ~720 m above the surface (Stephens *et al.*, 2008). Over land, surface clutter effects are not as easily removed resulting in greater uncertainty in detecting clouds and drizzle at low-levels (Marchand *et al.*, 2008; Christensen *et al.*, 2013). Therefore, ground-based systems continue to provide key observations of clouds and precipitation over the lowest levels of the atmosphere (e.g., Feingold *et al.*, 2003).

This paper provides a preliminary overview of the unique radar observations of cloud and precipitation systems made by the Aerosol, Cloud, Humidity Interactions Exploring and Validation Enterprise (ACHIEVE) mobile laboratory during its inaugural deployment in northern Vietnam during the spring 2013 Seven Southeast Asian Studies/Biomass-burning Aerosols & Stratocumulus Environment: Lifecycles & Interactions Experiment (7-SEAS/BASELInE) campaign. ACHIEVE is part of NASA Goddard Space Flight Center's Surface-based Mobile Atmospheric Research and Testbed Laboratories (SMARTLabs, http://smartlabs.gsfc.nasa.gov). As these observations are the first of their kind for this region, a critical first step to understanding the potential impacts of aerosols on these cloud systems is to analyze the cloud systems themselves. Initial results from numerical cloud simulations with advanced microphysics examining aerosol-cloud interactions over this region are also presented.

OBSERVATIONAL ACTIVITIES

The ACHIEVE mobile laboratory operated at the regional meteorological station in Yen Bai, Vietnam (21.705°N, 104.87°E) from 25 March through 10 April 2013. Yen Bai is situated roughly 50 m above sea level and approximately 120 km west-northwest of Hanoi in northern Vietnam (Fig. 1). A small mountain range oriented approximately SE-NW with elevations ranging from about 1.5 to 2.5 km is located roughly 50 km to the west. The site lies within a BB aerosol-cloud confluence region during the pre-monsoon months (*cf.* Tsay *et al.*, 2013), and is thus a prime location for observing aerosols and clouds in an effort to better understand the fundamentals of their interactions.

The initial goal was to have ACHIEVE operating at Yen Bai beginning around 1 March 2013 and continue through early April to coincide with the transition period from dry to pre-monsoon season, as well as the onset of peak burning season over western SEA. However, storms in the Pacific Ocean delayed ACHIEVE's arrival in Vietnam by several weeks. Once ACHIEVE was set up at Yen Bai, power to the site was frequently interrupted due to ongoing upgrades of the local electrical transmission system resulting in data gaps for all instruments. Despite these setbacks, this inaugural deployment of ACHIEVE was a great success, capturing numerous low-level Sc events and creating a unique dataset of cloud systems over this underrepresented region.

ACHIEVE Instrumentation

ACHIEVE contains an integrated suite of active and passive remote sensing instruments for measuring the structures and properties of clouds and precipitation, as well as retrieving columnar aerosol and atmospheric properties, from a ground-based platform. Fig. 3(a) shows the setup of ACHIEVE at Yen Bai. The active instruments include a scanning W-band (93.93 GHz) dual polarization Doppler cloud radar, a vertically-pointing K-band (24 GHz) Micro Rain Radar (MRR), and a 910 nm ceilometer. ACHIEVE's W-band radar exhibits great sensitivity (e.g., –53 dBZ at 1 km range for 25 m range resolution), and can be configured to transmit and receive in either short pulse mode or pulse compression mode, with the latter permitting increased sensitivity and range resolution. The MRR measures Doppler spectra and estimates radar reflectivity profiles, Doppler velocities, and path integrated attenuation. Additionally, retrievals of rain rate and liquid water content are possible with a stated minimum detectable threshold of 0.01 mm hr^{-1}

for rain rate. The Vaisala CL51 ceilometer uses a 910 nm wavelength laser to measure vertical profiles of attenuated backscatter up to 15 km and infer cloud base height for up to three cloud layers.

Passive instruments include an Atmospheric Emitted Radiance Interferometer (AERI), and a sun photometer (part of the Aerosol Robotic Network, AERONET). AERI measures absolute radiances of downward thermal emissions over the spectral range of about 3 to 18 µm at 1 cm^{-1} resolution. Data products include sky brightness temperatures at measured wavenumbers, along with retrievals of aerosol and bulk cloud properties, and profiles of temperature, pressure and humidity under cloud-free sky conditions, as well as below cloud under cloudy conditions. Unforeseen problems with AERI's data processing software following 7-SEAS/BASELInE have unfortunately precluded use of this data at the time of this writing. An upgraded AERONET sun photometer measures polarized radiances at 9 channels ranging from 340 to 1640 nm and operates in both cloud-free and cloud mode. Data include spectral aerosol optical depth along with retrievals of aerosol size distributions in cloud-free conditions, and retrieved cloud optical depth when operating in cloud mode. Table 1 provides the specifications and data products for ACHIEVE instrumentation that operated during the 2013 7SEAS/BASELInE deployment.

The W-band radar operated mostly in vertically-pointing mode throughout the campaign in order to capture the evolution of cloud and precipitation system vertical structures as they passed overhead. The scanning strategy also included hourly Range Height Indicator (RHI) scans at E-W, SE-NW, and S-N azimuth angles and spanning 45–135° elevation, as well as Plan Position Indicator (PPI) scans at 60–85° elevation in increments of 5° in an effort to sample spatial variability of the systems. Full hemispheric scans were not
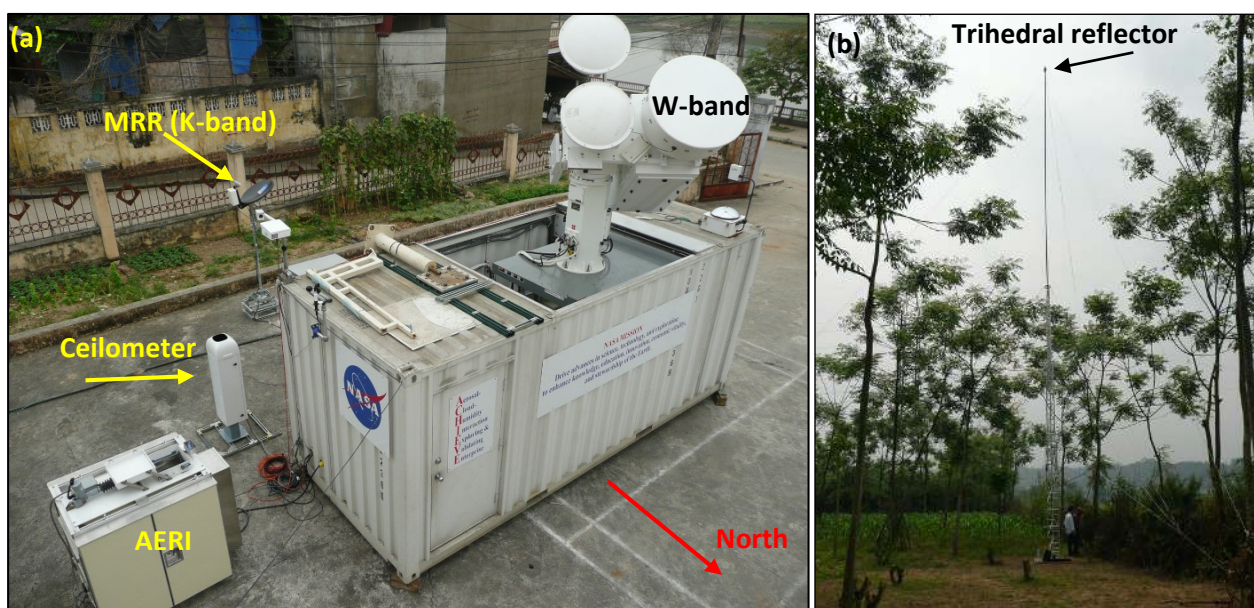

Fig. 3. a) Set up of ACHIEVE at Yen Bai regional meteorological station, Yen Bai, Vietnam. Red arrow indicates orientation. AERONET sun photometer was located in a grassy area roughly 40 m north of ACHIEVE. b) Photo of the 10 m aluminum calibration tower with an additional 10 m carbon fiber mast atop which sits a 16.25 cm trihedral corner reflector.

Table 1. ACHIEVE instrument descriptions for 2013 7SEAS/BASELInE deployment.

INSTRUMENT	DESCRIPTION/SPECIFICATIONS	PRODUCTS
W-band (93.93 GHz) radar	-scanning dual-polarization (single-pol transmit, dual-pol receive) Doppler cloud radar -beamwidth: 0.25° -minimum noise equivalent reflectivity: –53 dBZ at 1 km -uncertainty: ± 1 dB -dynamic range: ~80 dB -min/max range: 0.48/8.4 km -resolution: 25 m -integration time: 1.1 s for vertical-pointing, 0.13 s for RHI/PPI scans	Range-dependent Doppler spectra, equivalent radar reflectivity, Doppler mean velocity and spectral width, linear depolarization ratio (LDR), signal-to-noise ratio (SNR)
CL-51 ceilometer	-910 nm lidar -max range: 15 km -nominal range: 7 km -resolution: 10 m	Range-dependent total attenuated backscatter; boundary layer depth, cloud base height (up to 4.5 km)
K-band (24 GHz) Micro Rain Radar (MRR)	-vertically pointing Frequency Modulated Continuous Wave (FM-CW) precipitation radar -beamwidth: 1.5° -max range: 1.1 km -resolution: 35 m -minimum detectability: ~–5 dBZ (Maahn and Kollias, 2011)	Range-dependent Doppler spectra, mean Doppler velocity, path integrated attenuation; retrievals of range-dependent equivalent radar reflectivity, rain rate, liquid water content
Atmospheric Emitted Radiance Interferometer (AERI)	-measures absolute radiances of downward thermal emissions -spectral range: 3–20 μm (continuous) -spectral resolution: 1 cm^{-1}	-sky brightness temperatures; retrievals of aerosol and cloud properties; temperature, pressure and humidity profiles
Sun photometer	-measures polarized radiances over atmospheric column at 9 channels (8 aerosol + 1 water vapor) -spectral range: 340–1640 nm (discrete) -cloud-free and cloud mode operation	-spectral aerosol optical depth (AOD); aerosol size distributions; cloud optical depth (COD) for cloud mode only

possible due to the presence of nearby buildings. The radar moment data (reflectivity, mean Doppler velocity, and spectral width) were computed from the range-dependent Doppler power spectra after subtracting out the mean noise power (i.e., average of sky noise samples taken during the spectra averaging period). In addition, moment data having signal to noise ratios less than 5 dB were excluded from analyses presented herein. Given the narrow beamwidth and high elevation angles (> 45°) of the radar above the horizon for this deployment, ground clutter echo contamination was negligible. Radar reflectivity was not corrected for gaseous attenuation, although this should be minimal for vertically-pointing mode. Attenuation by liquid water was also not performed as this requires information on the particle size distributions. On-site calibration of the W-band radar was performed at the beginning and mid-way through the deployment using a 16.25 cm trihedral corner cube reflector mounted atop a 20 m tall portable tower located 370 m to the west of ACHIEVE (Fig. 3(b)).

Summary of ACHIEVE Observations

Throughout ACHIEVE's deployment, low-level Sc cloud decks observed over the Yen Bai region tended to follow a diurnal cycle. The cloud layer usually developed in the mid to late evening, thickened and occasionally developed drizzle or light rain overnight. The low-level Sc would generally linger through the early to mid-morning and eventually dissipate by mid-day as the boundary layer warmed. This diurnal cycle is evident in Contoured Frequency with Altitude Diagrams (CFADs; Yuter and Houze, 1995) of ACHIEVE's W-band reflectivity data collected from 28 March through 9 April 2013 (Figs. 4(a)–4(d)). These diagrams depict the probability density of a field as a function of height and were constructed by partitioning the observed reflectivity values into 5-dBZ bins beginning at –30 dBZ for each height. The data were further partitioned into four 6-hour time periods (07:00–13:00, 13:00–19:00, 19:00–01:00, and 01:00–07:00, all times local) and normalized by the number of profiles in each respective time period in order to depict the diurnal cycle. The greater probabilities of radar echos above –20 dBZ observed below 2 km for the nighttime periods (19:00–07:00 local; Figs. 4(c) and 4(d)) point to more frequent occurrences of low-level cloudiness during the night versus daytime in agreement with the CALIPSO cloud mask feature frequency profiles (*cf*. Fig. 1(b)). The CFADs also depict well the development of nighttime precipitation as evident the sloped region of peak probabilities that increases from –15 dBZ near 1.8 km to between 0 and 10 dBZ at the
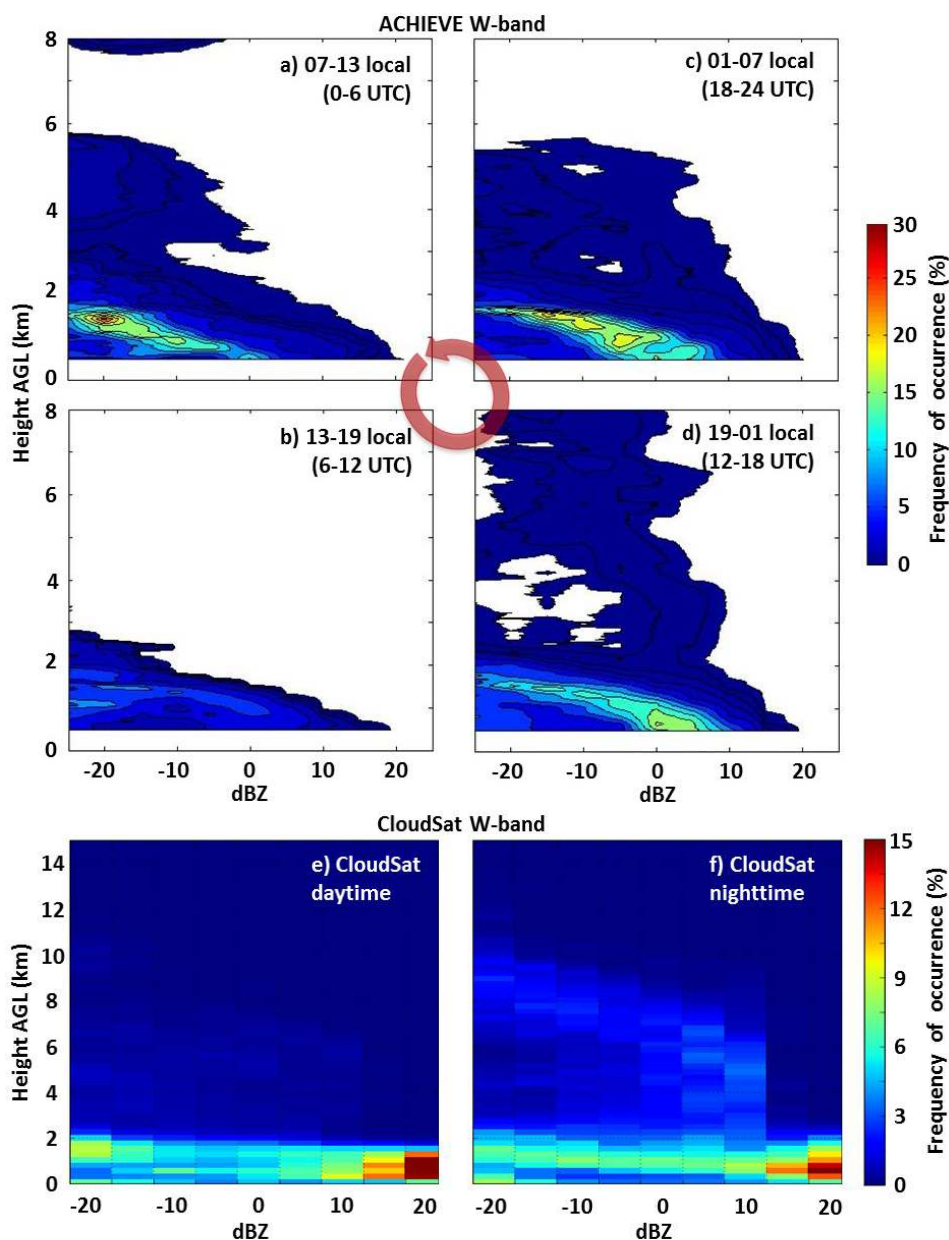
Fig. 4. Contoured Frequency with Altitude Diagrams (CFADs) computed from ACHIEVE's W-band radar reflectivity for the time period spanning 28 March through 9 April 2013 (panels a–d) and from CloudSat/CPR overpasses within 100 km of Yen Bai, Vietnam for the months of March and April for the years 2007–2012 (panels e and f). Data from both instruments is further partitioned into daytime (left column) and nighttime (right column), with ACHIEVE W-band CFADs further partitioned into 6-hour increments as listed in each panel (UTC times given in parentheses) whose sequence is denoted by the circular red arrow. Note different height and frequency scales are used for ACHIEVE and CloudSat CFADs.

lowest levels in Figs. 4(c) and 4(d). Physically, this sloped feature results from the growth of drops as they fall through the cloud layer towards the surface (Li *et al.*, 2008; Mechem *et al.*, 2011). Mid- and high-level clouds were also more prevalent overnight as shown by increased probabilities of echoes above roughly 3 km relative to the daytime period. These echoes were mostly associated with elevated convective systems that passed over the region on several occasions, yet their contribution to total cloudiness during the deployment was minimal as evident by the low magnitudes of probability (~2.5%) relative to the peaks

(~17.5%) at low levels.

Reflectivity CFADS constructed from all available CloudSat/CPR overpasses within 100 km of Yen Bai during March and April for the years 2007–2012 are also presented in Figs. 4(e) and 4(f). The CPR's minimum detectability is around –28 dBZ (Stephens *et al.*, 2002), although this generally corresponds to features above the moist atmospheric boundary layer. As such, reflectivity values below –25 dBZ were not included for this particular analysis due to increased noise in the CPR signal near the Earth's surface. Slightly greater probabilities of cloud echoes around 2 km,

as well as more frequent mid- and high-level clouds, are seen for night versus daytime; however, nominal overpass times around 01:30 and 13:30 local suggest that the diurnal cycle of low-level clouds is not well represented (Mace and Zhang, 2014). Peak probabilities in the CloudSat/CPR CFADs occur around 1 km height and for values greater than 15 dBZ; however, these most likely result from surface contamination (Marchand *et al.*, 2008) and are therefore associated with large uncertainties regarding the presence of low-level clouds.

An example of the radar reflectivity time series from ACHIEVE's W-band radar on 9 April 2013 (Fig. 5(b)) shows in detail a persistent low-level Sc cloud deck between roughly 1.1–1.6 km height in addition to cumulus underneath stratus as revealed by the occasional gaps in reflectivity ~1 km. Variability in the ceilometer-indicated cloud-base height arises primarily from scattered cumulus clouds passing over the measurement site. Radar reflectivity values below the ceilometer-indicated cloud-base denote very light precipitation (virga) falling from the cloud, whereas sudden dips in the ceilometer-indicated cloud-base height (e.g., ~05:00–05:13) may indicate pannus (or stratus fractus), which can form in association with localized precipitation below clouds. For this particular time period, no clouds were present above the Sc deck, no surface precipitation was observed on site, surface temperatures ranged between ~18–20°C, and near-surface winds were out of the east and less than 5 m s^{-1}. Light rain had fallen earlier in the day between roughly 02:30–03:00 UTC, although the Sc deck existed both prior to and after this brief rain episode. Concurrent measurements made by CALIPSO and CloudSat/CPR satellites during a nearby overpass around 06:30 UTC reveal a layer consisting of fine mode aerosols existed above the low-level Sc deck (Figs. 5(c) and 5(d)), yet the CPR missed the majority of low-level Sc over the Yen Bai region (Fig. 5(a)). This particular example highlights the

advantages of ground-based over space-borne radar for studying detailed cloud and precipitation structures and processes in low-level clouds.

Fig. 6 shows an excellent example of the typical diurnal evolution of low-level Sc over Yen Bai as observed by ACHIEVE's W-band cloud radar on 7–8 April 2013. The cloud deck first develops around 1.5 km between 13:00–18:00 UTC (20:00 7 April–01:00 8 April local time), thickening to several hundred meters by 16:00 UTC. The evolving cloud deck is dominated by cloud-sized particles (diameter, $D <$ 50 μm, reflectivity values below –15 dBZ) and downward Doppler velocities are mostly less than 0.7 m s^{-1}, typical thresholds used to delineate non-drizzling from drizzling Sc (Sauvageot and Omar, 1987; Fox and Illingsworth, 1997; Löhnert *et al.*, 2001). Given that such small particles have negligible fall velocities (primarily due to turbulent eddies in vertical motion), they can act as tracers within the environmental flow. Thus, the mean radial velocities shown in Fig. 7 represent the along-beam component of this horizontal flow within the cloud layer, and imply flow from the southeast to the northwest, perpendicular to the axis of zero (or minimal) radial velocity (Doviak and Zrnić, 1993). Weak radar echo returns (< –30 dBZ) below 1 km prior to 18:00 UTC are due primarily to insects.

By 18:00 UTC (01:00 local), formation of a secondary cloud deck is evident near 800 m. Development of light drizzle is evident in the RHI scan (Fig. 6(d)) between 0 and 1 km distance SE, and appears as increasing reflectivity downward from cloud top to near cloud base as growing droplets near cloud top subsequently fall and grow *via* coalescence, as described by Fox and Illingsworth (1997). The NW to SE slope of this "drizzle streak" is likely due to the fact that as the drizzle drops grow in size, they attain greater fall speeds and deviate more from the environmental flow. The RHI and PPI reflectivity scans (Figs. 6(c) and 6(d)) depict considerable spatial variability of the cloud properties.
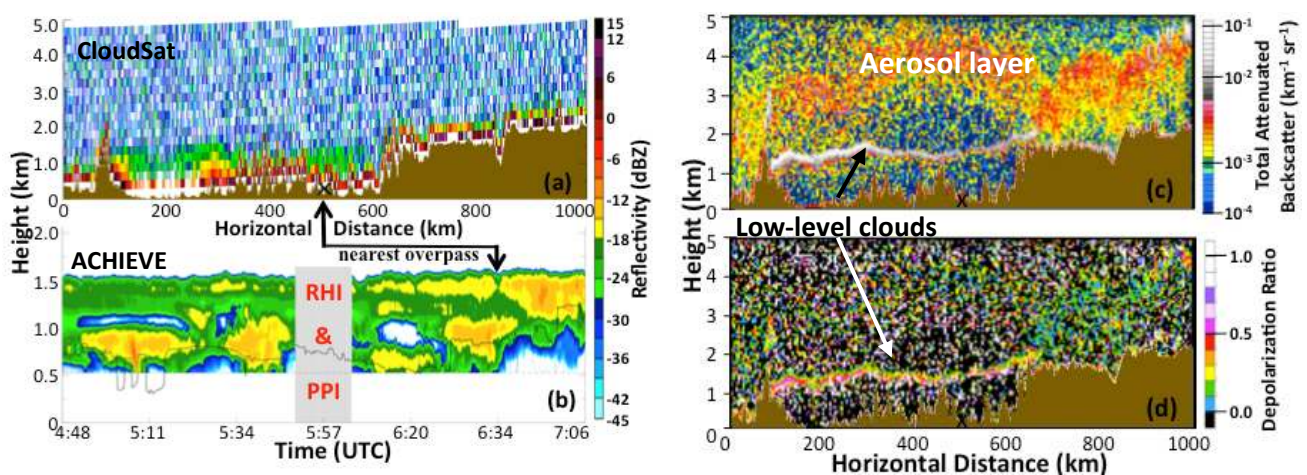

Fig. 5. On 9 April 2013, showing a) along-track CloudSat/CPR reflectivity (dBZ) in 06:33–06:35 UTC (yellow line superimposed on Fig. 1a image), with 'arrow' denoting time of the nearest (~57 km) CloudSat overpass to Yen Bai (symbol X), b) time series of ACHIEVE's vertically-pointing W-band co-polar radar reflectivity, using same color scales in (a), with ceilometer-detected cloud-base height (solid black line), c) collocated A-Train CALIPSO/CALIOP backscatter profiles indicating low-level clouds with aerosols aloft, and d) as in (c) but for volume depolarization ratio featuring water clouds and fine-mode aerosols aloft.
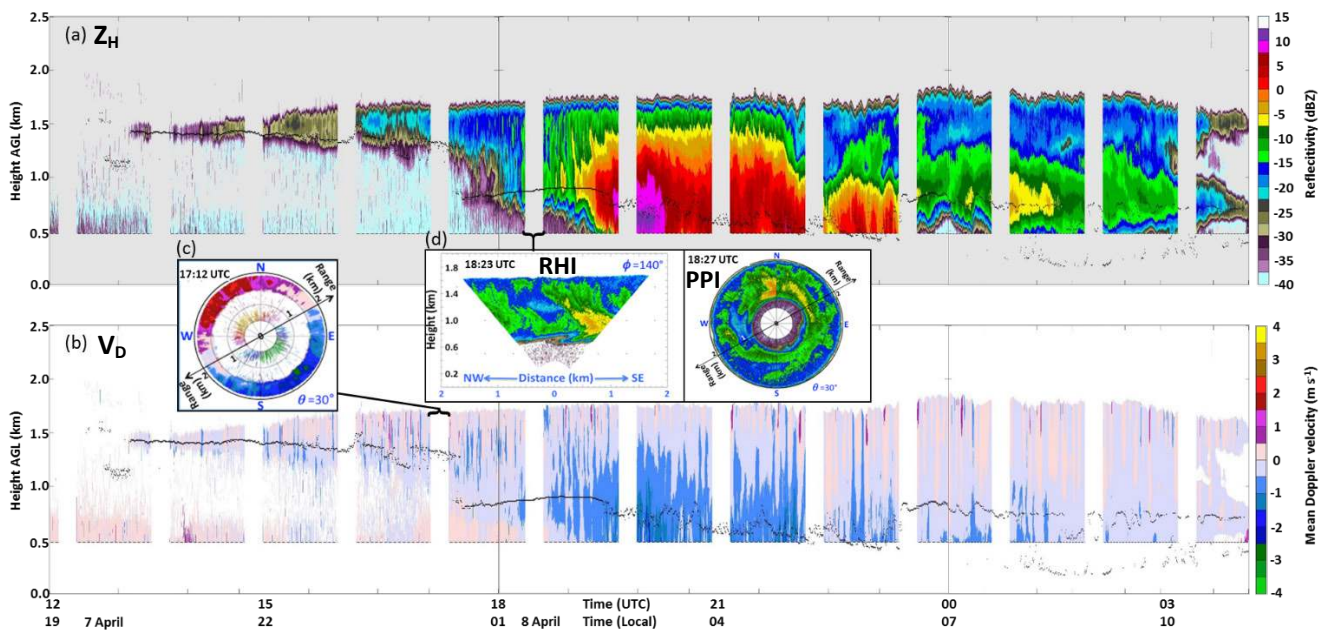
Fig. 6. Time-height contour plots of (a) co-polar reflectivity, Z_H, and (b) mean Doppler velocity, V_D, measured by vertically-pointing W-band radar on 7–8 April 2013 (local time 19:00 7 April to 04:00 8 April 2013) over Yen Bai, Vietnam. The dashed line in (a) and (b) near 0.5 km indicates the minimum detection range of the radar, breaks denote time periods of radar operating in RHI (range-height indicator) and PPI (plan-position indicator) scanning modes, and ceilometer-derived cloud base heights are indicated by black dots. (c) Mean radial velocity measured by PPI cone-scanning (17:12 UTC at 30° zenith angle), showing cloud-level flow is generally from the southeast to the northwest. (d) RHI slice-scanning (18:23 UTC at 140° azimuth and between ± 45° zenith angles) and PPI cone-scanning (18:27 UTC at 30° zenith angle) of radar reflectivity reveal the drizzle formation and fallout phase of the Sc deck.
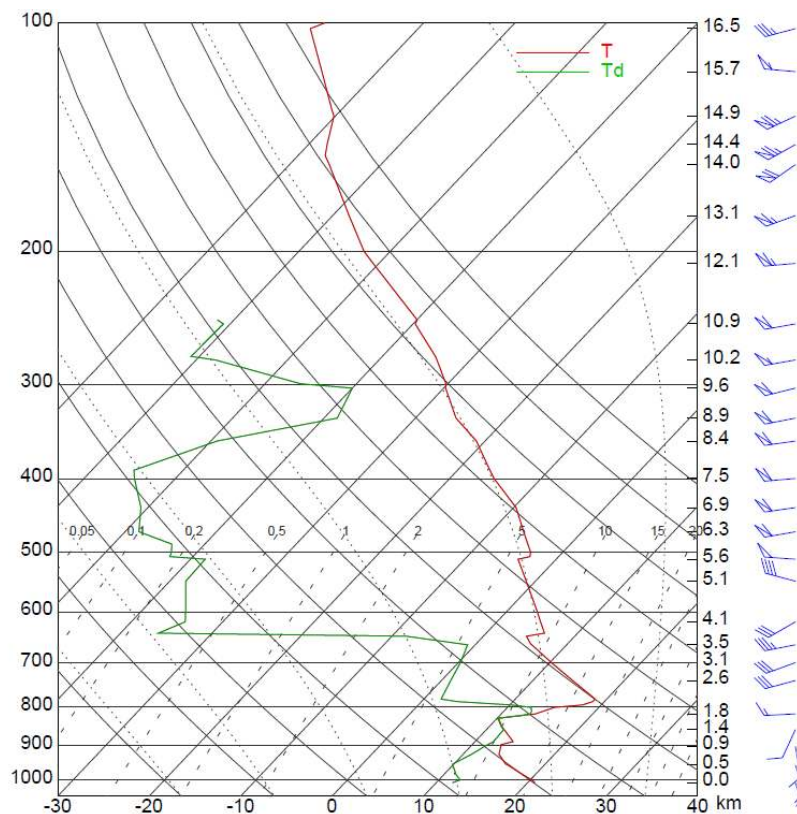

Fig. 7. Skew-T diagram for 1200 UTC sounding for Hanoi, Vietnam on 7 April 2013 used to initialize aerosol sensitivity simulations.

A period of moderate drizzle occurs between 19:30 and 22:00 UTC (02:30–05:00 local) as depicted by increases in reflectivity magnitudes (Fig. 6(a)) and downward mean Doppler velocities (Fig. 6(b)), with peak magnitudes of 11 dBZ and –2 m s^{-1}, respectively, around 20:00 UTC (03:00 local). Assuming the environmental vertical velocity is near zero and neglecting turbulent contributions, these mean Doppler velocity values correspond to mean drop diameters around 0.1 to 0.2 mm based on diameter-fallspeed relationships from Mitchell (1996) thereby placing these drops in the large drizzle to small raindrop size range. It is important to note, however, that the Doppler velocities include vertical air motion and turbulence, both of which are unknown without additional measurements. Reflectivity time series from the vertically-pointing MRR indicated only a trace of precipitation (< 0.1 mm) actually reached the surface (not shown); however, given the lower frequency, wider beamwidth, and much lower power of the MRR relative to the W-band, the weak intensity of the drizzle is likely underdetected (Maahn and Kollias, 2012). Beyond 22:00 UTC (05:00 local), drizzle production ceases and the two cloud decks become increasingly distinct from one another with time. Both cloud layers begin to dissipate by 04:00 UTC (11:00 local).

PRELIMINARY MODEL WORK

Measurements from 7-SEAS/BASELInE provide insight into the microphysical, chemical, and radiative properties associated with aerosol-cloud interactions for Sc over land (Tsay *et al.*, 2013). To enhance our understanding of the relative importance of the roles played by microphysical and macrophysical processes in the different cloud regimes and at different stages within the cloud's lifecycle, synergistic combination of observed aerosol/cloud properties with comprehensive modeling efforts are essential. A critical first step in this process is to employ high-resolution cloud models capable of simulating the underlying small-scale physical processes in aerosol-cloud interactions before attempting to interpret the measurements taken at different times and locations over the broader region.

GCE Model Overview

The Goddard Cumulus Ensemble (GCE) model is a nonhydrostatic cloud-resolving model developed and maintained at NASA/GSFC as part of the larger Goddard Multi-scale Modeling System with Unified Physics (Tao *et al.*, 2009, 2014). Simulations can be performed in either 2D or 3D and can be forced by soundings or large-scale tendencies such as from regional-scale model output or reanalysis data. Subgrid-scale turbulent transport of energy and mass associated with boundary-layer clouds (i.e., stratocumulus) is predicted *via* turbulent kinetic energy (TKE, Klemp and Wilhelmson, 1978; Soong and Ogura, 1980) or optional Smagorinsky dynamic (Kirkpatrick *et al.*, 2006) schemes and is also coupled with land and ocean models to provide surface fluxes of heat and moisture. Short- and long-wave radiative transfer processes, as well as their interactions with aerosols and clouds, are computed

for eight bands each across the solar and infrared spectrum (Chou and Suarez, 1999; Chou *et al.*, 1999), respectively.

The GCE model's single-moment bulk microphysical schemes are based on Lin *et al.* (1983) with various modifications/improvements (Tao *et al.*, 2003; Lang *et al.*, 2014). The GCE model additionally incorporates the single-moment (1M) and double-moment (2M) versions of Colorado State University's Regional Atmospheric Modeling System (RAMS) bulk microphysical scheme (Meyers *et al.*, 1997; Saleeby and Cotton, 2004, 2008) as well as a spectral bin microphysical scheme (Khain *et al.*, 2004). Bin schemes are advantageous over bulk models in representing processes such as particle nucleation, collision-coalescence, and sedimentation by explicitly predicting the evolution of hydrometeors of discrete sizes, at considerable computational expense however. Bulk schemes employ analytical distribution functions to represent hydrometeor distributions and predict distribution characteristics such as mass mixing ratio q (related to the 3rd moment), particle concentration N_t (related to the 0th moment), and/or spectral width (v). The modified gamma distribution (Ulbrich, 1983) is commonly used in cloud studies since it adequately represents many cloud/rain drop size distributions (CDSD) measured by *in-situ* probes and disdrometers (Miles *et al.*, 2000; Brandes *et al.*, 2003). Furthermore, this distribution function permits variability in CDSDs due to aerosols acting as CCN that affect cloud droplet sizes, number concentrations, and distribution spectral widths (e.g., Liu *et al.*, 2008; Martins and Silva Dias, 2009).

One issue with 1M- and 2M-bulk schemes is the inability to account for changes in the spectral width (v) of the size distributions resulting from microphysical processes such as droplet activation, collection, sedimentation, melting, and evaporation. With the exception of melting, these processes are critical in assessing the aerosol-cloud-precipitation interactions of stratocumulus clouds (e.g., Sundu *et al.*, 2008; Wood, 2012). Milbrandt and Yau (2005) developed a triple-moment (3M) bulk microphysics scheme that predicts the sixth moment (related to the radar reflectivity factor) of precipitating hydrometeor size distributions in addition to q and N_t in order to obtain time-dependent v values. Loftus *et al.* (2014) developed and implemented a similar 3M scheme into the RAMS model, and an enhanced version of this scheme that extends 3M prediction to cloud and rain distributions has recently been integrated into the GCE. The prediction of v for cloud and precipitating hydrometeor distributions allows for a more complete assessment of aerosol effects on droplet sizes, numbers, and the spectral width/shape of the distributions. In turn, the 3M scheme results in improved simulation of microphysical processes and allows for more accurate calculations of simulated active/passive signals (e.g., Dawson *et al.*, 2010; Kollias *et al.*, 2011; Loftus, 2012), which can then be used to gauge model performance against both ground-based and satellite observations as well as to provide insight into various physical processes (Matsui *et al.*, 2014).

The bulk 3M microphysics scheme has also been incorporated into the Goddard Satellite Data Simulator Unit (G-SDSU) to account for variability in v when computing

radar reflectivity from the predicted hydrometeor fields. The G-SDSU is a forward radiation model coupled to the GCE that permits interfacing remote-sensing/in-situ measurements with model output (Matsui *et al.*, 2009; Masunaga *et al.*, 2010; Matsui *et al.*, 2013). The resultant meteorological and geophysical parameters simulated by the GCE are used as inputs to G-SDSU to drive the individual instrument simulators for calculating radiance, reflectivity and backscattered Level-1b signals.

Simulations of 7 April 2013 Case

The 7 April 2013 case was selected as a '*golden scenario*' case to gauge the ability of the recently implemented 3M scheme to simulate the early developmental stage of low-level Sc over land. Due to the processing data issues with retrieving atmospheric profiles from AERI, the 12:00 UTC atmospheric sounding from Hanoi (Fig. 7) was used as a proxy for the atmospheric state over Yen Bai just prior to the time at which the first cloud echoes were observed. A small increase in vapor mixing ratio was applied to the 850 to 820 mb layer to force a slightly supersaturated (0.05%) layer in which clouds could develop. The model domain

was initialized horizontally homogenously and no additional forcing was applied. Because this was a nighttime case, the absence of shortwave radiative impacts of aerosols and clouds simplifies the interpretation of results. Table 2 lists the model parameter settings applied in the simulations.

Six simulations were performed in which number concentrations of aerosols (N_a) acting as potential CCN were systematically increased from surface maximum values of 100 to 2000 cm^{-3} (Fig. 8) to examine the impacts on the modeled clouds. The upper limit of this range was selected to correspond with *in-situ* surface aerosol measurements taken at Son La, Vietnam (about 110 km west-southwest of Yen Bai) prior to 7 April. Analyses of back trajectories using the NOAA HYSPLIT model (Draxler and Rolph, 2015) for the deployment period revealed air parcels in the 1.5 to 3 km layer above the Yen Bai region generally arrived from the southwest and west (not shown), such that they often traversed the Son La region. As Son La and Yen Bai are situated along the long-range transport path of BB aerosols (*cf.* Fig. 2 of Tsay *et al.*, 2013), it is reasonably assumed that the aerosols were aged sufficiently (i.e., more hygroscopic) and hence suitable to serve as CCN (Reid *et*

Table 2. Specification of key GCE model parameters used in this study.

| MODEL PARAMETER	SPECIFICATION
Domain size	14 × 14 × 13.6 km
Grid spacing	Horizontal: Δx = Δy = 200 m Vertical: 30 m lowest level stretched to approximately 300 m above 13 km
Time steps (time-splitting method of Klemp and Wilhelmson, 1978)	Large: 1 s Small (acoustic): 0.25 s
Boundary conditions	Open lateral Flat no-slip bottom, rigid top with sponge layer
Microphysics	New 3M bulk scheme based on Loftus *et al.* (2014)
Radiation	Chou and Suarez, 1999; Chou *et al.*, 1995, 1999
Subgrid turbulence	1.5 order TKE
Land flux model	Off
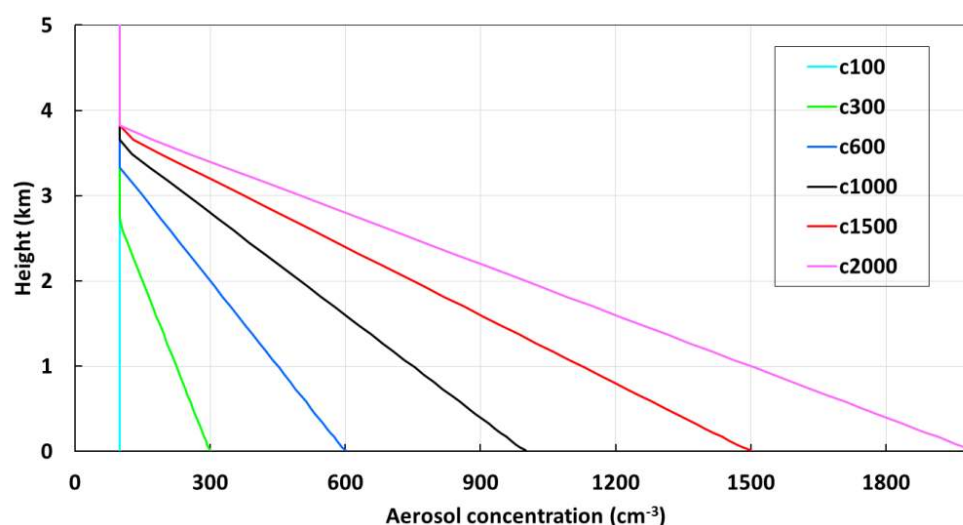
Fig. 8. Names and corresponding aerosol number concentration profiles for the six sensitivity simulations performed. Naming convention is associated with maximum aerosol concentration at the surface.

al., 2005). Aerosol distributions in all cases were assigned a dry mean mass diameter of 0.13 μm, within the range of values (0.12 to 0.18 μm) from sun photometer retrievals at Yen Bai as well as *in-situ* measurements upstream at Son La, and a fractional solubility of 50% as a proxy for aged BB aerosols.

The highly idealized nature (i.e., no forcing beyond the imposed supersaturation) and identical environmental conditions in these simulations help ensure that differences in cloud microphysical responses in each case are due primarily to changes in N_a. As neither *in-situ* measurements of aerosol/CCN nor profiles of these particles are available at Yen Bai during the 2013 7-SEAS/BASELInE campaign, results from these particular simulations are not intended to draw specific conclusions regarding the effects of BB aerosols on the observed cloud system, but rather to serve as a guideline for potential impacts of aerosols on these clouds and how the impacts might be 'observed' from a remote sensing standpoint.

Preliminary Simulation Results

Time-height plots of cloud droplet number concentrations (N_c), cloud droplet effective radius (r_e) and simulated W-band attenuated reflectivity (Z) at the domain mid-point

represent the evolution of the modeled cloud layer for selected aerosol sensitivity simulations (Fig. 9). Because the supersaturated layer spans roughly 1.4 and 1.7 km, cloud droplets nucleate within this layer upon model startup in all cases. The cloud layer slowly thickens over roughly the next two hours, with cloud tops extending to near 2 km by 16 UTC in each simulation (Fig. 9). As expected, increases in N_a lead to greater values of N_c (Figs. 9(a)–9(d)) and smaller r_e (Figs. 9(e)–9(h)) in accordance with the 'first aerosol indirect effect' (Twomey, 1977; Rosenfeld and Lensky, 1998; Andreae *et al.*, 2004). Values of N_c even at high N_a conditions are small (< 50 cm^{-3}) relative to typical observed values for Sc over land (Miles *et al.*, 2000) most likely due to lower supersaturation values in the absence of any organized vertical motion. The evolution of Z in the cases shown (Figs. 9(i)–9(l)) matches well with the early stages of the observed Sc deck (Fig. 6, prior to ~18 UTC) in terms of magnitudes and vertical extent, although the simulated cloud decks are shifted upwards by 200 to 300 m relative to the observations. Development of a second, lower cloud layer does not occur in the simulations due to the fixed environmental conditions. A decrease in Z of approximately 2.5 dBZ is seen as N_a increases from 300 to 2000 cm^{-3} during the initial development stage (Figs. 9(i)–9(l), 14–16
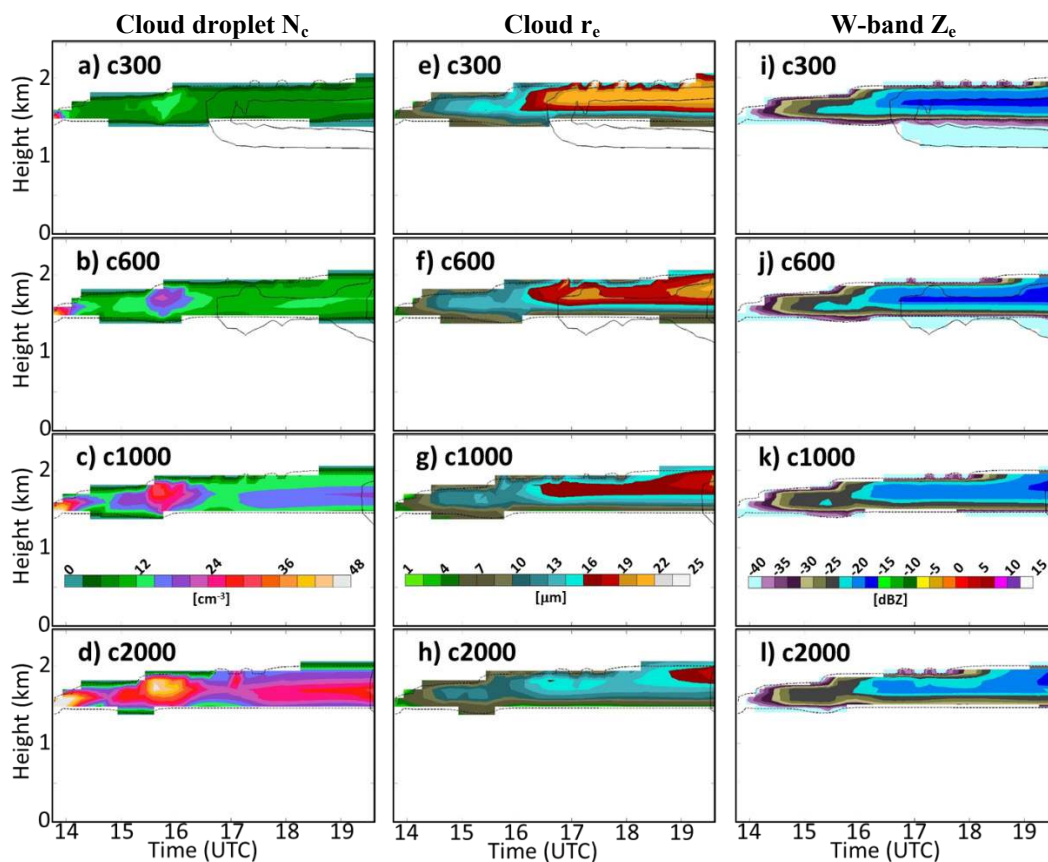

Fig. 9. Time-height plots of (left column) cloud droplet number concentrations N_c [cm^{-3}], (middle column) cloud droplet effective radius r_e [μm], and (right column) simulated W-band equivalent radar reflectivity values Z_e [dBZ] for selected aerosol sensitivity simulations of 7 April 2013 case. Cloud (drizzle/rain) liquid water content values of 1×10^{-2} (1×10^{-4}, 1×10^{-5}) g m^{-3} are overlaid as dashed (solid) black contours in each panel. Radar reflectivity values computed for ground-based radar using G-SDSU.

UTC), with a weaker trend of decreasing reflectivity with increasing N_a evident beyond about 16 UTC. The negative correlation between N_a and Z results largely from decreases in droplet sizes with increasing N_a.

Very light drizzle (rain water contents of order 10^{-4} to 10^{-5} g m^{-3}) develops in the lower aerosol loading cases (c300 and c600) beyond roughly 17 UTC associated with $Z \geq -18$ dBZ (Figs. 9(i) and 9(j)), within the –20 to –15 dBZ range typically used to distinguish drizzling from non-drizzling Sc (e.g., Sauvageot and Omar, 1987; Löhnert *et al.*, 2001; Kogan *et al.*, 2005). While such low rain water content values seem negligible, they are non-trivial from a microphysical modeling standpoint as they represent a small, yet quantifiable transition from a non-precipitating to a precipitating category. Shallow regions of weak reflectivity values (< –37.5 dBZ) immediately below cloud base in these cases depict virga, whereas reduced rain water contents and reflectivity values in cases c1000 and c2000 (Figs. 9(k) and 9(l)) suggest drizzle formation is suppressed. It is noted that drizzle production is inefficient even at low N_a values. Such inefficiency results from shallow cloud depth, low cloud LWP values (*cf.* Fig. 10(a)), and lack of large scale forcing (e.g., upward vertical motion within the cloud layer does not exceed 0.1 m s^{-1} in all simulations, not shown). As vertical motion is absent initially, local buoyancy perturbations due to condensation and evaporation of droplets create turbulent motions that maintain the cloud layer. Lee *et al.*, (2009) also noted dominance of condensation and evaporation over droplet self-collection and accretion in clouds with low LWP under weakly forced conditions. Although aerosol removal processes are not included in these simulations, the suppression of drizzle at greater N_a values infers little to no impact on the boundary layer air quality in these particular scenarios given that precipitation scavenging of aerosols below cloud base is proportional to precipitation rate (Pruppacher and Klett, 1997; Seinfeld and Pandis, 1998).

Time series of domain-averaged total LWP and cloud optical depth (τ_c) for all simulations (Fig. 10) show that LWP and τ_c values increase steadily as the cloud deck develops, reach a plateau signifying a more or less quasi-equilibrium state for roughly two hours, then begin to increase again. There is an increasing delay in reaching quasi-equilibrium

state as N_a increases. The reason for this behavior is linked to the growth of the droplets within a limited reservoir of water vapor. The more numerous cloud droplets, activated under higher N_a conditions, leads to faster reduction in supersaturation due to more rapid growth rates of smaller droplets and more vigorous competition for available water vapor (Yum and Hudson, 2005). The plots also reveal an increase in these radiatively important parameters as N_a increases in agreement with the original model of Albrecht (1989), although there is little noticeable difference in cloud thickness as has been suggested for marine Sc (e.g., Pincus and Baker, 1994). This result agrees with the initial increases in LWP and τ_c with increasing N_a seen for simulations of non-drizzling nocturnal marine Sc by Sundu *et al.* (2008), but is opposite to decreases in these cloud parameters reported by Jiang *et al.* (2002), Wang *et al.* (2003), and Hill *et al.* (2008, 2009). Ackerman *et al.* (2004) and Lee *et al.* (2009) showed that decreased LWP under higher aerosol loading scenarios were largely due to increased entrainment of overlying dry air and evaporation of droplets within updrafts near cloud top. Given the extremely weak vertical motion in the current simulations, a plausible explanation for increasing LWP with increasing aerosol loading is the apparent lack of entrainment of dry air from above cloud top.

CONCLUDING REMARKS AND FUTURE WORK

The 2013 7-SEAS/BASELInE campaign involved the first ever deployment of a ground-based millimeter cloud radar to the northern Vietnam region in an effort to capture detailed evolution of low-level Sc layers over land in the presence of BB aerosols. As current satellite observations of this low-level Sc layer generally lack details on the cloud structure due to surface clutter effects and signal attenuation, ground-based observations continue to provide crucial measurements over the lower layers of the atmosphere. Despite a reduced data collection period (17 days versus the expected 5–6 weeks) and unplanned power interruptions, data collected by ACHIEVE's W-band radar and ancillary instrumentation provided the first-ever comprehensive ground-based measurements of low-level Sc systems over this particular region. Analyses of the W-band radar data revealed these cloud systems were generally
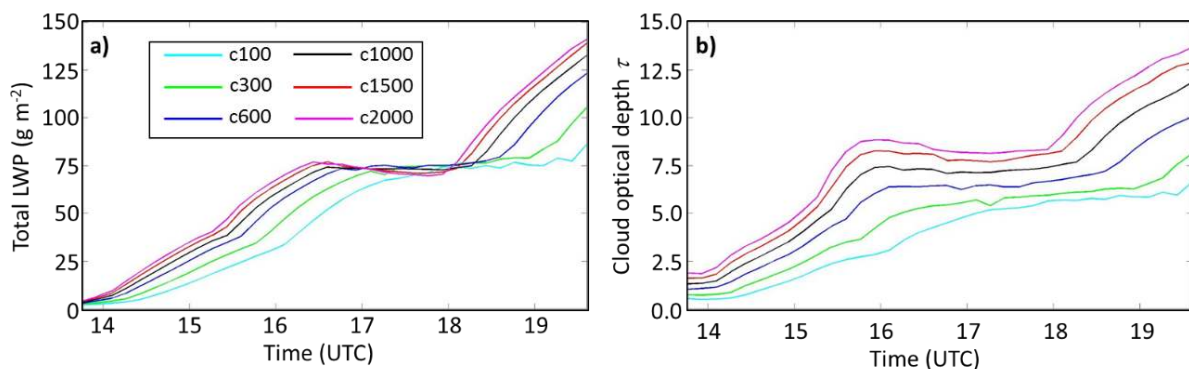

Fig. 10. Time series of domain-averaged a) total liquid water path (LWP, g m^{-2}) and b) cloud optical depth τ for aerosol sensitivity simulations of 7 April 2013 case.

confined to below 2 km and tended to follow a diurnal cycle, with peak occurrences during the nighttime and early morning hours, often accompanied by light precipitation. Future analyses will incorporate retrieved aerosol properties and profiles of atmospheric thermodynamic variables (T, RH, p) from the AERI data once the processing issue has been resolved. These data, along with regional reanalysis data, will permit more thorough understanding of the role of meteorology on the cloud system lifecycle, help determine the degree of coupling of the aerosol and cloud layer, and aid in estimations of precipitation impacts on local air quality via the aerosol washout effect.

A lack of concurrent aerosol data during cloudy episodes precludes a detailed examination of aerosol-cloud interactions from these particular observations, and thus, modeling efforts constrained by the available data are required to better understand potential impacts BB aerosols may have on the cloud system evolution. Previous investigations of aerosol impacts on low-level Sc have focused overwhelmingly on marine cloud systems, which are generally controlled by very different dynamical processes compared to systems over land (Mechem *et al.*, 2010; Wood, 2012). The preliminary results from aerosol sensitivity simulations presented herein revealed the familiar response of increased numbers and smaller sizes of cloud droplets with increasing aerosol concentrations, whereas increases in LWP and cloud optical depth were mostly opposite to findings from previous studies on marine Sc. Slight reductions in simulated W-band reflectivity values were seen with increasing aerosol concentrations and resulted primarily from decreased droplet sizes. Additionally, drizzle formation, albeit extremely small, was evident only for low aerosol loading cases in agreement with previous studies.

There are certainly shortcomings of the highly idealized simulations presented herein, and efforts are currently underway to alleviate some of the model deficiencies with respect to the representation of aerosol processes within the GCE model. In particular, the RAMS bulk aerosol module (Saleeby and van den Heever, 2013) simulates aerosol removal via cloud droplet nucleation and wet/dry deposition, and aerosol regeneration upon hydrometeor evaporation. Aerosol mass is also tracked within hydrometeors, and non-activated aerosols are advected with the model-predicted flow fields. This aerosol module was recently implemented into the GCE model and is currently undergoing compatibility tests within the larger GCE framework. The removal of atmospheric aerosols by nucleation and precipitation scavenging, as well as cloud processing of aerosols, are processes that impact local and regional air quality in addition to potential effects on cloud and precipitation evolution downstream (Levin and Cotton, 2009; Flossman and Wobrock, 2010). Wet scavenging below cloud increases with rain rate and is most efficient for aerosol particles with diameters D_a ≤ ~0.05 μm, as well those with D_a ≥ ~2–3 μm, whereas aerosols within the "Greenfield Gap" ($0.1 \leq D_a \leq 1$ μm) are most effectively removed via cloud droplet nucleation (Seinfeld and Pandis, 1998; Andronache, 2003; Feng, 2007). Relationships between below-cloud scavenging efficiency and radar reflectivity (e.g., Jylhä, 1999), as well as dependencies

of scavenging efficiency on rain drop distribution characteristics (e.g., Jung *et al.*, 2003), also suggest the need for accurate representation of hydrometeor distributions such as with the 3M scheme used herein. Another key aspect of this module is the use of a species-dependent soluble fraction parameter, ε, which accounts for aerosol hygroscopicity in a manner analogous to the κ-parameter (Petters and Kreidenweis, 2007, 2008). For example, smaller (larger) values of ε can be applied to represent freshly emitted (aged) biomass-burning aerosols. Future simulations will also incorporate time-dependent meteorological forcing based output from week-long simulations over the SEA region using the Weather Research and Forecasting model coupled with Chemistry (WRF-Chem) (Grell *et al.*, 2005; Fast *et al.*, 2006). Aerosol emissions, transport, and aging processes predicted by WRF-CHEM and constrained by collaborative 7-SEAS/BASELInE measurements (e.g., Lin *et al.*, 2013; Tsay *et al.*, 2013; Lin *et al.*, 2014) will further permit more realistic aerosol input into the GCE.

The knowledge and experience gained regarding instrument capabilities and sampling requirements for obtaining cloud and aerosol measurements during 7-SEAS/BASELInE and subsequent campaigns have led the SMARTLabs team to develop a more comprehensive approach for addressing aerosol-cloud interactions. Planning is currently underway for a follow-on experiment in the coming years as part of the ongoing 7-SEAS campaign to deploy SMARTLabs' ACHIEVE and Chemical, Optical, and Microphysical Measurements of *In-situ* Troposphere (COMMIT, *cf.* Pantina *et al.*, 2016) mobile laboratories to the Yen Bai region in conjunction with AERONET, Micro Pulse Lidar Network (MPLNET) and regional contributing instruments. The addition of an Unmanned Aerial Vehicle (UAV) equipped with microphysics and aerosol probes for sampling in-cloud and near-cloud environments, particularly cloud-clear air interface regions, is also possible (Tsay *et al.*, 2016). This multinational collaborative effort will permit co-located remote sensing and in-situ measurements of thermodynamic, aerosol and cloud profiles that will greatly aid in synergistic analyses of the observational data, as well as provide critical constraints for continued development and evaluation of models and retrievals aimed at improving our understanding of aerosol-cloud interactions.

ACKNOWLEDGEMENTS

REFERENCES

Ackerman, A.S., Kirkpatrick, M.P., Stevens, D.E. and Toon, O.B. (2004). The impact of humidity above stratiform clouds on indirect aerosol climate forcing. *Nature* 432: 1014–1017.

Albrecht, B. (1989). Aerosols, cloud microphysics, and fractional cloudiness. *Science* 245: 1227–1230.

Andreae, M.O., Rosenfeld, D., Artaxo, P., Costa, A.A., Frank, G.P., Longo, K.M. and Silva-Dias, M.A. (2004). Smoking rain clouds over the Amazon. *Science* 303: 1337–1342.

Andronache, C. (2003). Estimated variability of below-cloud aerosol removal by rainfall for observed aerosol size distributions. *Atmos. Chem. Phys.* 3: 131–143.

Babb, D.M., Verlinde, J. and Albrecht, B.A. (1999). Retrieval of cloud microphysical parameters from 94-GHz radar Doppler power spectra. *J. Atmos. Oceanic Technol.* 16: 489–503.

Brandes, E.A., Zhang, G. and Vivekanandan, J. (2003). An evaluation of a drop distribution-based polarimetric radar rainfall estimator. *J. Appl. Meteorol.* 42: 652–660.

Chou, M.D. and Suarez, M. (1999). A Solar Radiation Parameterization for Atmospheric Studies. NASA Technical Memorandum, NASA/TM-1999-104606, Vol. 15.

Chou, M.D., Lee, K.T., Tsay, S.C. and Fu, Q. (1999). Parameterization for cloud longwave scattering for use in atmospheric models. *J. Clim.* 12: 159–169.

Christensen, M.W., Stephens, G.L. and Lebsock, M.D. (2013). Exposing biases in retrieved low cloud properties from CloudSat: A guide for evaluating observations and climate data. *J. Geophys. Res.* 118: 12120–12131.

Clothiaux, E.E., Miller, M.A., Albrecht, B.A., Ackerman, T.P., Verlinde, J., Babb, D.M., Peters, R.M. and Syrett, W.J. (1995). An evaluation of a 94-GHz radar for remote sensing of cloud properties. *J. Atmos. Oceanic Technol.* 12: 201–229.

Crutzen, P.J. and Andreae, M.O. (1990). Biomass burning in the Tropics: Impact on atmospheric chemistry and biogeochemical cycles. *Science* 205: 1669–16678.

Dawson II, D.T., Xue, M., Milbrandt, J.A. and Yau, M.K. (2010). Comparison of evaporation and cold pool development between single-moment and multimoment bulk microphysics schemes in idealized simulations of tornadic thunderstorms. *Mon. Weather Rev.* 138: 1152–1171.

Doviak, R.J. and Zrnić, D.S. (1993). *Doppler Radar and Weather Observations*. 2nd Ed. Academic Press.

Draxler, R.R. andRolph, G.D. (2015). HYSPLIT (HYbrid Single-Particle Lagrangian Integrated Trajectory) Model access via NOAA ARL READY Website http://ready.arl.noaa.gov/HYSPLIT.php. NOAA Air Resources Laboratory, Silver Spring, MD.

Dusek, U., Frank, G.P., Hildebrandt, L., Curtius, J., Schneider, J., Walter, S., Chand, D., Drewnick, F., Hings, S., Jung, D., Borrmann, S. and Andreae, M.O. (2006). Size matters more than chemistry for cloud nucleating ability of aerosol particles. *Science* 312: 1375–1378.

Endo, N., Matsumoto, J. and Lwin, T. (2009). Trends in precipitation extremes over Southeast Asia. *SOLA* 5: 168–171.

Engelhart, G.J., Hennigan, C.J., Miracolo, M.A., Robinson, A.L. and Pandis, S.N. (2012). Cloud condensation nuclei activity of fresh primary and aged biomass burning aerosol. *Atmos. Chem. Phys.* 12: 7285–7293.

Fast, J.D., Gustafson, W.I., Easter, R.C., Zaveri, R.A., Barnard, J.C., Chapman, E.G., Grell, G.A. and Peckham, S.E. (2006). Evolution of ozone, particulates, and aerosol direct forcing in an urban area using a new fully-coupled meteorology, chemistry, and aerosol model. *J. Geophys. Res.* 111: D21305.

Feingold, G., Eberhard, W.L., Veron, D.E. and Previdi, M. (2003). First measurements of the Twomey indirect aerosol effect using ground-based remote sensors. *Geophys. Res. Lett.* 30: 1287.

Feingold, G., Jiang, H. and Harrington, J.Y. (2005). On smoke suppression of clouds in Amazonia. *Geophys. Res. Lett*. 32: L02804.

Feingold, G., McComiskey, A., Rosenfeld, D. and Sorooshian, A. (2013). On the relationship between cloud contact time and precipitation susceptibility to aerosol. *J. Geophys. Res.* 118: 10544–10554.

Feng, J. (2007). A 3-mode parametrization of below-cloud scavenging of aerosols for use in atmospheric dispersion models. *Atmos. Environ.* 4: 6808–6822.

Flossman, A.I. and Wobrock, W. (2010). A review of our understanding of the aerosol-cloud interaction from the perspective of a bin resolved cloud scale modelling. *Atmos. Res*. 97: 478–497.

Fox, N.I. and Illingworth, A.J. (1997). The retrieval of stratocumulus cloud properties by ground-based cloud radar. *J. Appl. Meteorol.* 36: 485–492.

Gautam, R., Hsu, N.C., Eck, T.F., Holben, B.N., Janjai, S., Jantarach, T., Tsay, S.C. and Lau, W.K. (2013). Characterization of aerosols over the Indochina peninsula from satellite-surface ob-servations during biomass burning pre-monsoon season. *Atmos. Environ.* 78: 51–59.

Graf, H.F., Yang, J. and Wagner, T.M. (2009). Aerosol effects on clouds and precipitation during the 1997 smoke episode in Indonesia. *Atmos. Chem. Phys*. 9: 743–756.

Grell, G.A., Peckham, S.E., Schmitz, R., McKeen, S.A., Frost, G., Skamarock, W.C. and Eder, B. (2005). Fully coupled 'online' chemistry within the WRF model. *Atmos. Environ.* 39: 6957–6976.

Hill, A.A., Dobbie, S. and Yin, Y. (2008). The impact of aerosols on non-precipitating marine stratocumulus. I: Model description and prediction of the indirect effect. *Q. J. R. Meteorolog. Soc*. 134: 1143–1154.

Hill, A.A., Feingold, G. and Jiang, H. (2009). The influence of entrainment and mixing assumption on aerosol-cloud interactions in marine stratocumulus. *J. Atmos. Sci.* 66:

1450–1464.

Ho, T.M.H., Phan, V.T., Le, N.Q. andNguyen, Q.T. (2011). Extreme climatic events over Vietnam from observational data and RegCM3 projections. *Clim. Res.* 49: 87–100.

Hsu, N.C., Herman, J.R. and Tsay, S.C. (2003). Radiative impacts from biomass burning in the presence of clouds during boreal spring in Southeast Asia. *Geophys. Res. Lett.* 30: 1224.

Huang, K., Fu, J.S., Hsu, N.C., Gao, Y., Dong, X., Tsay, S.C. and Lam, Y.F. (2013). Impact assessment of biomass burning on air quality in Southeast and East Asia during BASE-ASIA. *Atmos. Environ.* 78: 291–302.

Jiang, H., Feingold, G. and Cotton, W.R. (2002). Simulations of aerosol-cloud-dynamical feedbacks resulting from entrainment of aerosol into the marine boundary layer during the Atlantic Stratocumulus Transition Experiment. *J. Geophys. Res.* 107: 4813.

Jung, C.H., Kim, Y.P. and Lee, K.W. (2003). A moment model for simulating raindrop scavenging of aerosols. *J. Aerosol Sci.* 34: 1217–1233.

Jylhä, K. (1999). Relationship between the scavenging coefficient for pollutants in precipitation and the radar reflectivity factor. Part I: Derivation. *J. Appl. Meteorol.* 38: 1421–1434.

Khain, A., Pokrovsky, A., Pinsky, M., Seifert, A. and Phillips, V. (2004). Simulation of effects of atmospheric aerosols on deep turbulent convective clouds using a spectral microphysics mixed-phase cumulus cloud model. Part I: Model description and possible applications. *J. Atmos. Sci.* 61: 2963–2982.

Kirkpatrick, M.P., Ackerman, A.S., Stevens, D.E. Mansour, and N.N. (2006). On the application of the dynamic Smagorinsky model to large-eddy simulations of the cloud-topped atmospheric boundary layer. *J. Atmos. Sci.* 63: 526–546.

Klein, S.A. and Hartmann, D.L. (1993). The seasonal cycle of low stratiform clouds. *J. Clim.* 6: 1587–1606.

Klemp, J.B. and Wilhelmson, R.B. (1978). The simulation of three-dimensional convective storm dynamics. *J. Atmos. Sci.* 35: 1070–1096.

Kogan, Z.N., Mechem, D.B. and Kogan, Y.L. (2005). Assessment of variability in continental low stratiform clouds based on observations of radar reflectivity, *J. Geophys. Res.* 110: D18205.

Kollias P., Szyrmer, W., Remillard, J. and Luke, E. (2011). Cloud radar Doppler spectra in drizzling stratiform clouds. Part II: Observations and microphysical modeling of drizzle evolution. *J. Geophys. Res.* 116: D13203.

Kollias, P., Clothiaux, E.E., Miller, M.A., Albrecht, B.A., Stephens, G.L. and Ackerman, T.P. (2007). Millimeter-wavelength radars: New frontier in atmospheric cloud and precipitation research. *Bull. Am. Meteorol. Soc.* 88: 1608–1624.

Lang, S.E., Tao, W.K., Chern, J.D., Wu, D. and Li, X. (2014). Benefits of a fourth ice class in the simulated radar reflectivities of convective systems using a bulk microphysics scheme. *J. Atmos. Sci.* 71: 3583–3612.

Lee, D., Sud, Y.C., Oreopoulos, L., Kim, K.M., Lau, W.K. and Kang, I.S. (2014). Modeling the influences of aerosols on pre-monsoon circulation and rainfall over Southeast Asia. *Atmos. Chem. Phys.* 14: 6853–6866.

Lee, S.S., Penner, J.E. and Saleeby, S.M. (2009). Aerosol effects on liquid-water path of thin stratocumulus clouds. *J. Geophys. Res.* 114: D07204.

Levin, Z. and Cotton, W.R. (2009). *Aerosol Pollution Impact on Precipitation*. A Scientific Review. Springer.

Li., Y., Zipser, E.J., Krueger, S.K. and Zulauf, M. (2008). Cloud-resolving modeling of deep convection during KWAJEX. Part I: Comparison to TRMM satellite and ground-based radar observations. *Mon. Weather Rev.* 136: 2699–2712.

Lin, N.H., Sayer, A.M., Wang, S.H., Loftus, A.M., Hsiao, T.C., Sheu, G.R., Hsu, N.C., Tsay, S.C. and Chantara, S. (2014). Interactions between biomass-burning aerosols and clouds over Southeast Asia: Current status, challenges, and perspectives. *Environ. Pollut.* 195: 292–307.

Lin, N.H., Tsay, S.C., Maring, H.B., Yen, M.C., Sheu, G.R., Wang, S.H., Chi, K.H., Chuang, M.T., Ou-Yang, C.F., Fu, J.S., Reid, J.S., Lee, C.T., Wang, L.C., Wang, J.L., Hsu, C.N., Sayer, A.M., Holben, B.N., Chu, Y.C., Nguyen, X.A., Sopajaree, K., Chen, S.J., Cheng, M.T., Tsuang, B.J., Tsai, C.J., Peng, C.M., Schnell, R.C., Conway, T., Chang, C.T., Lin, K.S., Tsai, Y.I., Lee, W.J., Chang, S.C., Liu, J.J., Chiang, W.L., Huang, S.J., Lin, T.H. and Liu, G.R. (2013). An overview of regional experiments on biomass burning aerosols and related pollutants in Southeast Asia: From BASE-ASIA and the Dongsha Experiment to 7-SEAS. *Atmos. Environ.* 78: 1–19.

Lin, Y.L., Farley, R.D. and Orville, H.D. (1983). Bulk parameterization of the snow field in a cloud model. *J. Clim. Appl. Meteorol.* 22: 1065–1092.

Liu, Y., Daum, P.H., Guo, H. and Peng, Y. (2008). Dispersion bias, dispersion effect, and the aerosol-cloud conundrum. *Environ. Res. Lett.* 3: 045021.

Loftus, A.M. (2012). A Triple-moment Bulk Hail Microphysics Scheme to Investigate the Sensitivities of Hail to Aerosols. Ph.D. dissertation, Dept. of Atmospheric Science, Colorado State Univ., http://digitool.library.col ostate.edu/R/.

Loftus, A.M., Cotton, W.R. and Carrió, G.G. (2014). A triple-moment hail bulk microphysics scheme. Part I: Description and initial evaluation. *Atmos. Res.* 149: 35–57.

Lohmann, U. and Feichter, J. (2005). Global indirect aerosol effects: A review. *Atmos. Chem. Phys.* 5: 715–737.

Löhnert, U., Crewell, S. and Simmer, C. (2001). Profiling cloud liquid water by combining active and passive microwave measurements with cloud model statistics. *J. Atmos. Oceanic Technol.* 18: 1354–1366.

Maahn, M. and Kollias, P. (2012). Improved Micro Rain Radar snow measurements using Doppler spectra post-processing. *Atmos. Meas. Tech.* 5: 2661–2673.

Mace, G.G. and Zhang, Q. (2014). The CloudSat radar-lidar geometrical profile product (RL-GeoProf): Updates, improvements, and selected results. *J. Geophys. Res.* 119: 9441–9462.

Marchand, R., Mace, G.G., Ackerman, T. and Stephens, G.

(2008). Hydrometeor detection using CloudSat-An earth-orbiting 94-GHz cloud radar. *J. Atmos. Oceanic Technol.* 25: 519–533.

Martins, J.A. and Silvas Dias, M.A.F. (2009). The impact of smoke from forest fires on the spectral dispersion of cloud droplet size distributions in the Amazonian region. *Environ. Res. Lett.* 4: 015002.

Martins, J.A., Silva Dias, M.A.F. and Gonçalves, F.L.T. (2009). Impact of biomass burning aerosols on precipitation in the Amazon: A modeling case study. *J. Geophys. Res.* 114: D02207.

Masunaga, H., Matsui, T., Tao, W.K., Hou, A.Y., Kummerow, C.D., Nakajima, T., Bauer, P., Olson, W.S., Sekiguchi, M. and Nakajima, T.Y. (2010). Satellite Data Simulator Unit (SDSU): A multi-sensor, multi-spectral satellite simulator package. *Bull. Am. Meteorol. Soc.* 91: 1625–1632.

Matsui, T., Iguchi, T., Li, X., Han, M., Tao, W.-K., Petersen, W., L'Ecuyer, T., Meneghini, R., Olson, W., Kummerow, C.D., Hou, A.Y., Schwaller, M.R., Stocker, E.F. and Kwiatkowski, J. (2013). GPM satellite simulator over ground validation sites. *Bull. Am. Meteorol. Soc.* 94: 1653–1660.

Matsui, T., Zeng, X., Tao, W.K., Masunaga, H., Olson, W. and Lang, S. (2009). Evaluation of long-term cloud-resolving model simulations using satellite radiance observations and multi-frequency satellite simulators. *J. Atmos. Oceanic Technol.* 26: 1261–1274.

Matsui, T., Santanello, J., Shi, J.J., Tao, W.K., Wu, D., Peters-Lidard, C., Kemp, E., Chin, M., Starr, D., Sekiguchi, M. and Aires, F. (2014). Introducing multisensory satellite radiance-based evaluation for regional Earth System modeling. *J. Geophys. Res.* 119: 8450–8475.

Mechem, D.B., Kogan, Y.L. and Schultz, D.M. (2010). Large-eddy observation of post-frontal continental stratocumulus. *J. Atmos. Sci.* 67: 3368–3383.

Mechem, D.B., Yuter, S.E. and de Szoeke, S.P. (2012). Thermodynamic and aerosol controls of southeast Pacific stratocumulus. *J. Atmos. Sci.* 69: 1250–1266.

Meyers, M.P., Walko, R.L., Harrington, J.Y. and Cotton, W.R. (1997). New RAMS cloud microphysics parameterization. II: The two-moment scheme. *Atmos. Res.* 45: 3–39.

Milbrandt, J.A. and Yau, M.K. (2005). A multimoment bulk microphysics parameterization. Part II: A proposed three-moment closure and scheme description. *J. Atmos. Sci.* 62: 3065–3081.

Miles, N.L., Verlinde, J. and Clothiaux, E.E. (2000). Cloud droplet size distributions in low-level stratiform clouds. *J. Atmos. Sci.* 57: 295–311.

Mitchell, D. (1996). Use of mass- and area-dimensional power laws for determining precipitation particle terminal velocities. *J. Atmos. Sci.* 53: 1710–1723.

Nguyen, D.N. and Nguyen, T.H. (2004). *Climate and climate Resources in Vietnam*. Agriculture Publishing House. (in Vietnamese).

Nguyen, V.T., Nguyen, T.H., Tran, T.P., Thi, T.H., Nguyen, T.L. and Vu, V.T. (2010). *Climate change and impact in Vietnam*. Publishing House of Science and Engineering. (in Vietnamese).

Pantina, P., Tsay, S.C., Hsiao, T.C., Loftus, A.M., Kuo, F., Ou-Yang, C.F., Sayer, A.M., Wang, S.H., Lin, N.H., Hsu, N.C., Janjai, S., Chantara, S. and Nguyen, A.X. (2016). COMMIT in 7-SEAS/BASELInE: Operation of and observations from a novel, mobile laboratory for measuring in-situ properties of aerosols and gases. *Aerosol Air Qual. Res.* 16: 2728–2741.

Petters, M.D. and Kreidenweis, S.M. (2007): A single parameter representation of hygroscopic growth and cloud condensation nucleus activity. *Atmos. Chem. Phys.* 7: 1961–1971.

Petters, M.D. and Kreidenweis, S.M. (2008). A single parameter representation of hygroscopic growth and cloud condensation nucleus activity – Part 2: Including solubility. *Atmos. Chem. Phys.* 8: 6273–6279.

Phan, V.T., Fink, A.H., Ngo-Duc, T., Trinh, T.L., Pinto, J.G., van der Linden, R. and Schubert, D. (2014). Observed Climate Variations and Change in Vietnam. In *EWATEC-COAST: Technologies for Environmental and Water Protection of Coastal Zones in Vietnam*. Meon, G., Pätsch M., Phuoc N.V. and Quan N.H. (Eds.), Contributions to 4th International Conference for Environment and Natural Resources, ICENR 2014. Cuvillier, Göttingen, Germany.

Pincus, R. and Baker, M.B. (1994). Effect of precipitation on the albedo susceptibility of clouds in the marine boundary layer. *Nature* 372: 250–252.

Platnick, S. and Twomey, S. (1994). Determining the susceptibility of cloud albedo to changes in droplet concentration with the advanced very high resolution radiometer. *J. Appl. Meteorol.* 33: 334–347.

Pruppacher, H.R. and Klett, J.D. (1997). *Microphysics of Clouds and Precipitation*. 2nd Ed. Kluwer Academic.

Reid, J.S., Koppmann, R., Eck, T.F. and Eleuterio, D.P. (2005). A review of biomass burning emissions part II: Intensive physical properties of biomass burning particles. *Atmos. Chem. Phys.* 5: 799–825.

Reid, J.S., Hyer, E.J., Johnson, R.S., Holben, B.N., Yokelson, R.J., Zhang, J., Campbell, J.R., Christopher, S.A., Di Girolamo, L., Giglio, L., Holz, R.E., Kearney, C., Miettinen, J., Reid, E.A., Turk, F.J., Wang, J., Xian, P., Zhao, G., Balasubramanian, R., Chew, B.N., Janjai, S., Lagrosas, N., Lestari, P., Lin, N.H., Mahmud, M., Nguyen, A.X., Norris, B., Oanh, N.T.K., Oo, M., Salinas, S.V., Welton, E.J. and Liew, S.C. (2013). Observing and understanding the Southeast Asian aerosol system by remote sensing: An initial review and analysis for the Seven Southeast Asian Studies (7SEAS) program. *Atmos. Res.* 122: 403–468.

Reutter, P., Su, H., Trentmann, J., Simmel, M., Rose, D., Gunthe, S.S., Wernli, H., Andreae, M.O. and Pöschl, U. (2009). Aerosol- and updraft-limited regimes of cloud droplet formation: Influence of particle number, size and hygroscopicity on the activation of cloud condensation nuclei (CCN). *Atmos. Chem. Phys.* 9: 7067–7080.

Rosenfeld, D. and Lensky, I.M. (1998). Satellite-based insights into precipitation formation processes in continental and maritime convective clouds. *Bull. Am.*

Meteorol. Soc. 79: 2457–2476.

Saleeby, S.M. and Cotton, W.R. (2004). A large-droplet mode and prognostic number concentration of cloud droplets in the Colorado State University Regional Atmospheric Modeling System (RAMS). Part I: Module descriptions and supercell test simulations. *J. Appl. Meteorol.* 43: 182–195.

Saleeby, S. and van den Heever, S.C. (2013). Developments in the CSU-RAMS aerosol model: Emissions, nucleation, regeneration, deposition, and radiation. *J. Appl. Meteorol. Clim.* 52: 2601–2622.

Sauvageot, H. and Omar, J. (1987). Radar reflectivity of cumulus clouds. *J. Atmos. Oceanic Technol.* 4: 264–272.

Sayer, A.M., Hsu, N.C., Hsiao, T.C., Pantina, P., Kuo, F., Ou-Yang, C.F., Holben, B.N., Janjai, S., Chantara, S., Wang, S.H., Loftus, A.M., Lin, N.H. and Tsay, S.C. (2016). In-situ and remotely-sensed observations of biomass burning aerosols at Doi Ang Khang, Thailand during 7-SEAS/BASELInE 2015. *Aerosol Air Qual. Res.* 16: 2786–2801.

Schmidt-Thomé, P., Nguyen, T.H., Pham, T.L., Jarva, J. and Nuottimäki, K. (2015). *Climate Change Adaptation Measures in Vietnam*. Development and Implementation. Springer International Publishing.

Seinfeld, J.H. and Pandis, S.N. (1998). *Atmospheric Chemistry and Physics*. Wiley, New York.

Soong, S.T. and Ogura, Y. (1980). Response of trade wind cumuli to large-scale processes. *J. Atmos. Sci.* 37: 2016–2036.

Sorooshian, A., Feingold, G., Lebsock, M.D., Jiang, H.L. and Stephens, G.L. (2009). On the precipitation susceptibility of clouds to aerosol perturbations. *Geophys. Res. Lett.* 36: L13803.

Stephens, G.L. and Greenwald, T.J. (1991). Observations of the Earth's radiation budget in relation to atmospheric hydrology. Part II: Cloud effects and cloud feedback. *J. Geophys. Res.* 96: 15325–15340.

Stephens, G.L., Vane, D.G., Boain, R.J., Mace, G.G., Sassen, K., Wang, Z., Illingworth, A.J., O'Connor, E.J., Rossow, W.B., Durden, S.L., Miller, S.D., Austin, R.T., Benedetti, A., Mitrescu, C. and CloudSat Science Team, T. (2002). The CloudSat Mission and the A-Train: A new dimension of space-based observations of clouds and precipitation. *Bull. Am. Meteorol. Soc.* 83: 1771–1790.

Stephens, G.L., Vane, D.G., Tanelli, S., Im, E., Durden, S., Rokey, M., Reinke, D., Partain, P., Mace, G.G., Austin, R., L'Ecuyer, T., Haynes, J., Lebsock, M., Suzuki, K., Waliser, D., Wu, D., Kay, J., Gettelman, A., Wang, Z. and Marchand, R. (2008). CloudSat mission: Performance and early science after the first year of operation. *J. Geophys. Res.* 113: D00A18.

Sundu, I., Brenguier, J.L., Geoffroy, O., Thouron, O. and Masson, V. (2008). Aerosol impacts on the diurnal cycle of marine stratocumulus. *J. Atmos. Sci.* 65: 2705–2718.

Tao, W.K., Simpson, J., Baker, D., Braun, S., Chou, M.D., Ferrier, B., Johnson, D., Khain, A., Lang, S., Lynn, B., Shie, C.L., Starr, D., Sui, C.H., Wang, Y. and Wetzel, P. (2003). Microphysics, radiation and surface processes in the Goddard Cumulus Ensemble (GCE) model. *Meteorol. Atmos. Phys.* 82: 97–137.

Tao, W.K., Anderson, D., Chern, J., Entin, J., Hou, A., Houser, P., Kakar, R., Lang, S., Lau, W., Peters-Lidard, C., Li, X., Matsui, T., Rienecker, M., Schoeberl, M.R., Shen, B.W., Shi, J.J. and Zeng, X. (2009). The Goddard multi-scale modeling system with unified physics. *Ann. Geophys.* 27: 3055–3064.

Tao, W.K., Lang, S., Zeng, X., Li, X., Matsui, T., Mohr, K., Posselt, D., Chern, J., Peters-Lidard, C., Norris, P.M., Kang, I.S., Choi, I., Hou, A., Lau, K.M. and Yang, Y.M. (2014). The Goddard Cumulus Ensem-ble (GCE) model: Improvements and applications for studying precipitation processes. *Atmos. Res.* 143: 392–424.

Tridon, F., Battaglia, A. and Kollias, P. (2013). Disentangling Mie and attenuation effects in rain using a Ka-W dual-wavelength Doppler spectral ratio technique. *Geophys. Res. Lett.* 40: 1–5.

Tsay, S.C., Hsu, N.C., Lau, W.K.M., Li, C., Gabriel, P.M., Ji, Q., Holben, B.N., Judd Welton, E., Nguyen, A.X., Janjai, S., Lin, N.H., Reid, J.S., Boonjawat, J., Howell, S.G., Huebert, B.J., Fu, J.S., Hansell, R.A., Sayer, A.M., Gautam, R., Wang, S.H., Goodloe, C.S., Miko, L.R., Shu, P.K., Loftus, A.M., Huang, J., Kim, J.Y., Jeong, M.J. and Pantina, P. (2013). From BASE-ASIA towards 7-SEAS: A satellite-surface perspective of boreal spring biomass-burning aerosols and clouds in Southeast Asia. *Atmos. Environ.* 78: 20–34.

Tsay, S.C., Maring, H.B., Lin, N.H., Buntoung, S., Chantara, S., Chuang, H.C., Gabriel, P.M., Goodloe, C.S., Holben, B.N., Hsiao, T.C., Hsu, N.C., Janjai, S., Lau, W.K.M., Lee, C.T., Lee, J., Loftus, A.M., Nguyen, A.X., Nguyen, C.M., Pani, S.K., Pantina, P., Sayer, A.M., Tao, W.K., Wang, S.H., Welton, E.J., Wiriya, W. and Yen, M.C. (2016). Satellite-surface perspectives of air quality and aerosol-cloud effects on the environment: An overview of 7-SEAS/BASELInE. *Aerosol Air Qual. Res.* 16: 2581–2602.

Twomey, S. (1977). The influence of pollution on the shortwave albedo of clouds. *J. Atmos. Sci.* 34: 1149–1152.

Ulbrich, C.W. (1983). Natural variations in the analytical form of the raindrop size distribution. *J. Clim. Appl. Meteorol.* 22: 1764–1775.

Wang, S., Wang, Q. and Feingold, G. (2003). Turbulence, condensation, and liquid water transport in numerically-simulated nonprecipitating stratocumulus clouds. *J. Atmos. Sci.* 60: 262–278.

Winker, D.M., Vaughan, M.A., Omar, A., Hu, Y., Powell, K.A., Liu, Z., Hunt, W.H. and Young, S.A. (2009). Overview of the CALIPSO mission and CALIOP data processing algorithms. *J. Atmos. Oceanic Technol.* 26: 2310–2323.

Wood, R. (2012). Review: Stratocumulus clouds. *Mon. Weather Rev.* 140: 2373–2423.

Yum, S.S. and Hudson, J.G. (2005). Adiabatic predictions and observations of cloud droplet spectral broadness. *Atmos. Res.* 73: 203–223.

Yuter, S.E. and Houze Jr., R.A. (1995). Three-dimensional

kinematic and microphysical evolution of Florida cumulonimbus. Part II: Frequency distributions of vertical velocity, reflectivity, and differential reflectivity. *Mon. Weather Rev.* 123: 1941–1963.